Efficient early global relaxation of asteroid Vesta

R. R. Fu, B. H. Hager, A. I. Ermakov, and M. T. Zuber

Abstract

The asteroid Vesta is a differentiated planetesimal from the accretion phase of solar system formation. Although its present-day shape is dominated by a non-hydrostatic fossil equatorial bulge and two large, mostly unrelaxed impact basins, Vesta may have been able to approach hydrostatic equilibrium during a brief early period of intense interior heating. We use a finite element viscoplastic flow model coupled to a 1D conductive cooling model to calculate the expected rate of relaxation throughout Vesta's early history. We find that, given sufficient non-hydrostaticity, the early elastic lithosphere of Vesta experienced extensive brittle failure due to self-gravity, thereby allowing relaxation to a more hydrostatic figure. Soon after its accretion, Vesta reached a closely hydrostatic figure with $<$2 km non-hydrostatic topography at degree-2, which, once scaled, is similar to the maximum disequilibrium of the hydrostatic asteroid Ceres. Vesta was able to support the modern observed amplitude of non-hydrostatic topography only $>$40-200 My after formation, depending on the assumed depth of megaregolith. The Veneneia and Rheasilvia giant impacts, which generated most non-hydrostatic topography, must have therefore occurred $>$40-200 My after formation. Based on crater retention ages, topography, and relation to known impact generated features, we identify a large region in the northern hemisphere that likely represents relic hydrostatic terrain from early Vesta. The long-wavelength figure of this terrain suggests that, before the two late giant impacts, Vesta had a rotation period of 5.02 hr (6.3% faster than present) while its spin axis was offset by 3.0° from that of the present. The evolution of Vesta's figure shows that the hydrostaticity of small bodies depends strongly on its age and specific impact history and that a single body may embody both hydrostatic and non-hydrostatic terrains and epochs.

1. Introduction

The terrestrial planets likely formed via the successive accretion of tens to hundreds of kilometer diameter objects known as planetesimals (Chambers, 2004). The high

abundance of short-lived radiogenic isotopes such as ^{26}Al in the early solar system led to the extensive interior melting of early-forming planetesimals. Thermal evolution models of planetesimals show that bodies as small as 20 km in diameter may have achieved >50% melting if accretion occurred sufficiently early (Hevey and Sanders, 2006; Elkins-Tanton et al., 2011; Šrámek et al., 2011). Such high degrees of melting led to full or partial differentiation of these bodies (McCoy et al., 2006).

Differentiated asteroids in the present-day solar system represent a relic population of these early-formed planetesimals. Vesta (mean diameter ∼525 km) is the best studied example of a differentiated asteroid. Ground-based spectroscopic studies have previously associated the surface of Vesta with meteorites of the howardite-eucrite-diogenite (HED) clan, whose geochemistries indicate igneous origins on a fully differentiated body (McCord et al., 1970; Binzel and Xu, 1993; Righter and Drake, 1997). More recently, the NASA Dawn mission, in orbit around Vesta between July 2011 and September 2012, deduced the presence of a metallic core with radius 110±3 km when assuming a core density similar to that of iron meteorites and measured surface spectra consistent with the HED meteorites (Russell et al., 2012; De Sanctis et al., 2012; Reddy et al., 2012).

Despite evidence for past interior and surface melting, present-day Vesta, similar to all asteroids except for Ceres, exhibits global-scale, non-hydrostatic topography. Orbital mapping of the Vestan surface has revealed the presence of two large (>400 km diameter) and relatively unrelaxed impact basins in the southern hemisphere (Marchi et al., 2012; Schenk et al., 2012). Furthermore, assuming a core and mantle with uniform densities, the current rotation rate of Vesta corresponds to a hydrostatic shape with flattening factor f_{eq} =0.13 (see Section 3.1). The flattening factor f is defined as $(a - c)/a$ where a and c are the equatorial and polar radii of the best-fit ellipsoid of revolution.

In contrast, the observed best-fit ellipsoid shows greater oblateness, with f ≈0.19 (Konopliv et al., submitted; Ermakov et al., submitted). This equatorial bulge of Vesta represents a non-hydrostatic fossil bulge; it cannot be explained by compensated topography as thickened, isostatically relaxed crust is expected to show a negative Bouguer anomaly. However, no such feature is observed at degree-2 (Ermakov et al., submitted). The correponding global disequilibrium factor $(f - f_{eq})$ of 0.07 is more than three orders of magnitude greater than the value for the Earth (Chambat et al., 2010). The impact basins and the non-hydrostatic bulge may have formed in the same giant impact events, which may contribute to topographic disequilibrium via direct redistribution of mass

and change to the rotation period or axis.

Unrelaxed global topography on Vesta and other asteroids is consistent with their low surface gravity and the high strength of cold silicates. Assuming a cool interior, large asteroids such as Vesta experience internal shear stresses on the order of $\sim$1 MPa due to disequilibrium topography and spin axis reorientation (Johnson and McGetchin, 1973; Matsuyama and Nimmo, 2011), which is insufficient to cause pervasive brittle failure even in previously fractured basaltic masses (Schultz, 1993). At the same time, viscous relaxation on asteroid-sized bodies with ambient temperatures of the present-day asteroid belt is expected to require much longer than the age of the solar system (Johnson and McGetchin, 1973).

However, given the high degree of past melting in differentiated asteroids such as Vesta, high shear stresses in a thin, chilled surface layer may have led to pervasive brittle failure and associated deformation during Vesta's early history. Likewise, the elevated temperatures may have allowed for viscous relaxation of topography on geologically short timescales.

Relaxation may have occurred on Vesta under two distinct scenarios (Fig. 1). In Relaxation Scenario One, Vesta may have relaxed from a non-hydrostatic shape in which it initially accreted. Although it is unclear whether Vesta and other planetesimals formed via large instabilities or incremental growth (Morbidelli et al., 2009; Weidenschilling, 2011), no accretion mechanism predicts formation in an already hydrostatic figure. As such, Vesta very likely accreted in a non-hydrostatic shape. Meanwhile, energy from the accretion process was likely insufficient to melt Vesta (Poitrasson et al., 2004; Šrámek et al., 2011). Vesta was therefore at first unable to relax from the non-hydrostatic figure in which it accreted. Short-lived radioactive isotopes subsequently heated the Vestan interior, leading to differentiation and a thin lithosphere on the order of one to several million years (Ghosh and McSween, 1998; Tang and Dauphas, 2012). Relaxation from the originally accreted shape to a closely hydrostatic one may have occurred at this time.

After the initial relaxation, large early impacts may have led to Relaxation Scenario Two. Such large impacts may have recreated significant non-hydrostatic topography during a brief early window; there is a 12-31% probability that Vesta was struck by a Rheasilvia basin-forming impactor sized object during the first 100 My (Davison et al., 2013). Because the cooling of the Vestan interior occurred gradually (see Section 2.2), Vesta would have been able to return to a closely hydrostatic figure if a large impact occurred sufficiently early. This relaxation may obscure the long wavelength topography

introduced by such early impacts, although the lack of compositionally distinct regions on the surface of Vesta excavated by such purported impacts suggests that they did not occur or that they occurred while igneous resurfacing on Vesta was still ongoing. As the interior of Vesta cooled, hydrostatic relaxation would have become impossible during its later history.

Topography on Vesta may therefore consist of a mixture of ancient terrains that achieved hydrostatic equilibrium during an early period of intense heating and late non-hydrostatic features acquired after Vesta cooled sufficiently to prevent further relaxation. Crater retention ages derived from Dawn observations show that the surface of Vesta indeed consists of both old and young terrains. The two large impact basins in Vesta's southern hemisphere are young features that have model ages of 2.1±0.2 (for the Veneneia basin) and 1.0±0.2 (Rheasilvia basin) Ga (Schenk et al., 2012). Meanwhile, the northern hemisphere of Vesta may have reached crater saturation and likely has not experienced catastrophic reshaping since early in Vesta's history (Marchi et al., 2012).

In this study, we use finite element models to evaluate the potential for hydrostatic relaxation on early Vesta and thereby assess the possibility that hydrostatic terrains exist on present-day Vesta. As described in Section 2, we construct numerical viscoplastic deformation models using the deal.II finite element libary (Bangerth et al., 2007). The flow model is coupled to a simple secular cooling model for Vesta that takes into account the effects of radiogenic heating and an insulating megaregolith layer. In Section 3, we report the expected extent of hydrostatic relaxation as a function of Vesta's age and assumed megaregolith thickness. We find that the global figure of early Vesta was much closer to hydrostatic equilibrium than observed today. We identify a large region in the northern hemisphere of Vesta as a likely relic of this early hydrostatic terrain and use its figure to constrain the rotation period and spin axis orientation of early Vesta. Finally, we discuss the implications of these results for the two late giant impacts and on the expected topography of other asteroids in Section 4.

2. Model Descriptions

2.1. Viscous relaxation model

To simulate the viscous relaxation of Vesta, we set up a numerical Stokes flow model in deal.II, an extensive and broadly applicable finite element library (Bangerth et al., 2007). We use an axisymmetic mesh consisting of between 5.8×10^3 and 1.2×10^4 quadrilateral cells with dimensions between 1.8 and 4.4 km and polynomial degree

1 shape functions (Fig. 2). The outer shape of the asteroid and the core mantle boundary are assumed to be ellipsoids of revolution. Symmetry of such bodies permits the simulation of the entire body by performing calculations on only one quadrant. Our solution mesh represents the body in the $x > 0$, $y > 0$ quadrant with the y and x axes corresponding to the polar and equatorial axes of the asteroid, respectively. On this mesh, we solve the Stokes equations, which govern incompressible flow where viscous forces dominate over inertial forces:

$$\partial_j(2\eta\dot{\epsilon}_{ij}) - \partial_i p = -g_i\rho$$

$$\partial_i u_i = 0 \tag{1}$$

where η is dynamic viscosity, p is pressure, ρ is density, u_i is flow velocity, and $\dot{\epsilon}_{ij}$ is the strain rate tensor defined as:

$$\dot{\epsilon}_{ij} = \frac{1}{2}\left(\partial_i u_j + \partial_j u_i\right). \tag{2}$$

The body acceleration g_i includes only contributions from self gravity and rotation. Self gravity is calculated analytically using the expressions for ellipsoids of revolution derived in Pohánka (2011). We apply zero pressure and zero traction boundary conditions to the outer surface of the asteroid. By symmetry, we specify the condition of zero normal velocity on the polar and equatorial axes of our domain.

We calculate the initial viscosity of all finite elements as a function of local temperature, which is approximately a function of depth from the surface of the asteroid (see Section 2.2). The true viscosity contrast between a molten interior and surface at space temperatures is well over 30 orders of magnitude (Solomatov, 2000). As in other finite element simulations of planetary interiors, such large viscosity contrasts create numerical instabilities in the solution [e.g., Moresi and Solomatov (1995)]. However, if the lowest specified interior viscosity is sufficiently small compared to the maximum near surface viscosity, the resulting global deformation field does not differ significantly from that calculated with the true, lower interior viscosity (Dombard and McKinnon, 2006). In such setups, the interior material is effectively inviscid and global deformation is controlled entirely by the high viscosity near-surface material. Therefore, at all nodes where the viscosity is lower than 2×10^{-5} times the maximum viscosity (η_{max}), we set the viscosity to $2 \times 10^{-5}\eta_{max}$. Changing this maximum contrast factor to 10^6 results in

less than 3% change in the resulting flow velocities.

Once the governing matrix equation is set up using the appropriate value for η, g_i, and ρ at each node, the stiffness matrix is first preconditioned using LU decomposition before solution is attempted. We then solve for pressure using an iterative conjugate gradient algorithm. Flow velocities are then calculated directly from the pressure solution (Bangerth and Kronbichler, 2008). Benchmark runs on rotating bodies of constant density and on non-rotating multi-layered bodies show that the analytic predictions for hydrostatic figures indeed minimize internal velocities and shear stresses as calculated from our finite element solution.

We account for brittle failure and plasticity in the early Vestan lithosphere. After each run of the finite element flow model, we calculate the local total stress tensor in each cell from the velocity and pressure solution:

$$\sigma_{ij} = 2\eta\dot{\epsilon}_{ij} - p\delta_{ij} \tag{3}$$

We then find the principal stresses by diagonalizing σ_{ij} using the Armadillo linear algebra library (Sanderson, 2010). We note that, for incompressible, isotropic media, the equation for elastic stress is isomorphic with Eq. 3. We find that our calculated stress fields in the early Vestan lithosphere agree closely ($<$10%) with the elastic model of Melosh (1977) at all depths, assuming a rigidity of 40 GPa in the high viscosity lid ($\eta > 10^{28}$ Pa s; see Section 2.2). Because the Melosh (1977) model applies only to figures with small deviation from equilibrium, the comparisons with this model are based on a Vesta with much smaller degree of disequilibrium ($f - f_{eq}$=0.005) than shapes used in this study (Section 3.1). The early Vestan crust was likely heavily fractured due to impactor bombardment (Davison et al., 2013), and fracture healing processes that operate on the Earth and the Moon likely did not occur as extensively on Vesta due to the asteroid's low interior pressures and absence of igneous activity after the first several 10s of My after Vesta's formation (Wieczorek et al., 2013; Yamaguchi et al., 1996). We therefore assume that the Vestan lithosphere is strengthless under extension (i.e., cohesionless). Where all principal stresses are compressive, we identify locations of brittle failure based on Byerlee's rule (Byerlee, 1978; Brace and Kohlstedt, 1980). Failure occurs in cells where the most compressive principal stress σ_1 exceeds $5\sigma_3$ where σ_3 is the least compressive principal stress.

A self-consistent viscoplastic solution requires that the stress tensor does not imply further brittle failure anywhere in the solution domain (Albert et al., 2000). We im-

plement plasticity using an iterative approach whereby the effective viscosity of each cell that experiences brittle failure is lowered after each iteration of the finite element flow model until no cells experience further failure (e.g., Kaus (2010); King and Hager (1990)). Physically, the effective viscosity accounts for displacement on fractures that are below the spatial scale resolved in the model (Dombard and McKinnon, 2006). We compute the new effective viscosity according to the equation:

$$\eta_{i+1}^{k} = \left(\frac{a\sigma_1^k}{b\sigma_3^k} \right)_i^{-1} \eta_i^k \tag{4}$$

where η_i^k represents the viscosity of cell k used during the ith iteration, b is a constant specifying the relationship between σ_1 and σ_3 upon failure (equal to 5 for Byerlee's rule), and a is a coefficient that is set to between 1 and 2 in order to control the rate of convergence. Varying a within this range does not affect the final viscosity structure upon convergence. The effective viscosity field after each run is smoothed at the 10-km scale to suppress numerical variations at the single cell level and to enhance model stability. Typically, 20 to 50 iterations were required to converge to an effective viscosity field that produces no significant further brittle failure. The viscous flow velocities of this resulting viscosity configuration represent the final viscoplastic relaxation rate of the body.

Each plasticity-corrected flow field solution represents the instantaneous viscoplastic relaxation rate for Vesta for a given shape and thermal structure. We simulate the time-dependent relaxation of Vesta by running simulations for a range of ages and degrees of disequilibrium. We interpolate these numerical results to find the instantaneous relaxation rate as a function of age and disequilibrium. The time-shape path of Vesta undergoing relaxation from an initial shape and age is then calculated with this interpolated function.

Our flow model does not incorporate elasticity and therefore does not account for additional elastically-supported displacement. Large elastic displacements may lead to significant changes in the gravity field of the body; this effect is not accounted for in our finite element model. However, the weak gravity field of Vesta implies that even thin lithospheres undergo only low-amplitude elastic deformation. Analytic estimates (Melosh, 1977) of elastic displacement for Vesta with the present-day degree of non-hydrostaticity indicate that a 20-km-thick lithosphere, which is thinner than the lithosphere thicknesses characteristic of early Vesta (see Section 3.1), allows less than 3 m of elastic displacement at the equator, assuming a rigidity of 40 GPa (Matsuyama

and Nimmo, 2011). This displacement is small compared to the ∼7 km displacement from equilibrium of modern Vesta and does not affect the gravity field.

An intact elastic layer of sufficient thickness can resist relaxation. However, for the high degrees of non-hydrostaticity modeled here, lithospheres on early Vesta undergo pervasive brittle failure and plastic deformation (see Section 3.1). Following Dombard and McKinnon (2006), we adopt an extended Maxwell rheology for the Vesta lithosphere:

$$\epsilon_{ij} = \epsilon_{ij,\,elastic} + \epsilon_{ij,\,viscous} + \epsilon_{ij,\,plastic} \tag{5}$$

where the total strain ϵ_{ij} is a sum of contributions from the three mechanisms. As such, although an unfractured, cold lithosphere on Vesta would undergo only minor elastic deformation, an extensively fractured lithosphere may undergo significant total deformation dominated by the plastic component.

2.2. Thermal evolution and base viscosity model

Due to the strong dependence of viscosity on temperature, the rate of viscous relaxation depends heavily on the thermal evolution of the asteroid interior. The initial heating of early-accreting asteroids smaller than ∼1000 km diameter is dominated by the decay of short-lived radionuclides, with impacts making a negligible contribution. Assuming cooling only by conduction, asteroids larger than 20-50 km diameter that accreted within 1.5 My of solar system formation[1] are expected to melt fully, except for a thin crust with thickness of order $\sqrt{\kappa\tau_{1/2}}$, where κ is the near-surface thermal diffusivity and $\tau_{1/2}$ is the half-life of ^{26}Al, the dominant heat source for early planetesimals (Šrámek et al., 2011). Using a value of $\kappa = 5 \times 10^{-7}$ m^2 s^{-1} for a fully sintered crust (Hanley et al., 1978) and $\tau_{1/2} = 7.17 \times 10^5$ years, the thickness of the unmelted crust is estimated to be ∼3 km. Intrinsic microporosity of chondritic material in the crust and additional macroporosity generated by impact brecciation may lower the value of κ by more than one order of magnitude (Warren and Rasmussen, 1987). Furthermore, the onset of melting in the asteroid interior would steepen the near surface thermal gradient (Hevey and Sanders, 2006). Both effects would lead to potentially much thinner crusts. The lack of primordial chondritic material on the Vestan surface also strongly suggests the past presence of extensive melting at shallow depths. On the other hand, accretion

[1]Here solar system formation is defined by the formation of calcium aluminum rich inclusions (CAIs) at 4.567 Ga (Amelin et al., 2002).

of Vesta some time (perhaps >1 My; Elkins-Tanton et al. (2011)) after the formation of CAIs would dramatically decrease its initial budget of short-lived radiogenic isotopes, leading to a thicker solid lid. We adopt an initial ∼10 km conductive lid as an upper bound that is in good agreement with numerical results for heating in Vesta (Ghosh and McSween, 1998).

We begin our conductive cooling model at the point of convective shut down. The uniform initial interior temperature is therefore chosen to be that at which the Vestan mantle ceases to support convective flow. The 10 km thick overlying lid is assumed to have a linear, conductive thermal profile (Fig. 3). We adopt 1200 ° C for the deep interior temperature, which is close to the rheological transition for dunite, the expected primary constituent of the Vestan mantle (Righter and Drake, 1997; Berckhemer et al., 1982). Below this temperature, rocks develop greater resistance to shear stress and would resist convection.

Due to this setup, all ages in our thermal evolution models refer to time after the cessation of convection. The duration of convection has been estimated to be <1 Myr and <<30 My (Neumann et al., submitted; Sterenborg and Crowley, 2012). Because this interval is short in comparison to the ages at which we run our finite element deformation models, the ages relative to the shutdown of mantle convection closely approximate those relative to the formation of Vesta. The overlying conductive lid is 10 km thick with top and bottom temperatures of -73 ° C and 1200 ° C, respectively. The surface temperature is chosen to be close to the black body temperature (188 K) for a rapid rotator at the current orbital radius of 2.36 AU. We note, however, that the thermal state of Vesta more than several 10s of My after initial formation is relatively insensitive to the initial thermal profile assumed and, instead, is a stronger function of the thermal diffusivity structure assumed.

Using this initial temperature profile, we create 1D numerical models of subsequent conductive cooling in a spherical geometry in *Mathematica*. We take into account heat generation from radionuclides and the different thermal diffusivities of the core, unbrecciated silicate, and megaregolith layers. This cooling process is governed by the diffusion equation in spherical coordinates (Haack et al., 1990):

$$\frac{\partial T}{\partial t} = \frac{W(t)}{c_p} + \frac{1}{r^2}\frac{\partial}{\partial r}\left[\kappa(r)\, r^2 \frac{\partial T}{\partial r}\right] \tag{6}$$

where $W(t)$ is the per unit mass heat production due to long-lived radioisotopes, c_p is the specific heat capacity, and $\kappa(r)$ is the thermal diffusivity that varies with radius.

We assume that Vesta has approximately Earth-like radioisotopic composition. The parameter $W(t)$ therefore consists mainly of contributions from the isotopes ^{232}Th, ^{238}U, ^{235}U, and ^{40}K, the last two of which have half-lives much shorter than the lifetime of the solar system. As a result, the total radiogenic heat flux from long-lived radionuclides decreased by a factor of $\sim$3 from 4.5 Ga to the present day. In our cooling model, we use a single exponentially decaying $W(t)$ that approximates the sum of contributions from the radioisotopes listed above (Turcotte and Schubert, 2002).

The insulating effect of high-porosity material at shallow depths can have a dramatic effect on the cooling rate of asteroids (Haack et al., 1990). As in the case of the Moon, the near-surface region of asteroids is expected to consist of finely-brecciated regolith overlying a deeper megaregolith consisting of fractured bedrock. The regolith layer may have thermal diffusivities up to two orders of magnitude lower than that of intact rock, while the thermal diffusivity of the megaregolith is $\sim$1 order of magnitude lower than that of the underlying bedrock. In the meantime, the metallic core of differentiated asteroids is expected to have a much higher thermal diffusivity and therefore a nearly isothermal temperature profile. We adopt thermal diffusivities of 2×10^{-5} m^2 s^{-1} for the metallic core, 5×10^{-7} m^2 s^{-1} for unbrecciated silicates, and 5×10^{-8} m^2 s^{-1} for the megaregolith (Hanley et al., 1978; Haack et al., 1990).

Although Dawn observations confirm the presence of a significant megaregolith layer on present-day Vesta (Denevi et al., 2012; Hoffmann et al., 2012), the thickness of the megaregolith layer is difficult to estimate. Meanwhile, impact modeling suggests that the depth of megaregolith on the lunar surface is approximately 2 km, or 0.1% of radius of the moon (Aggarwal and Oberbeck, 1979), although recent high-resolution gravity from the GRAIL mission (Zuber et al., 2013a) indicates that the lunar crust may be substantially more fractured than previously thought (Zuber et al., 2013b).

The depth of the megaregolith on asteroids may be signficantly greater due to the lower confining pressure. An early model for ejecta build up on large asteroids predicts between $\sim$1 and $>$4 km of megaregolith and regolith accumulated over the history of the solar system (Housen et al., 1979). A more recent model using a different assumed frequency of large impacts predicts that present-day megaregolith thickness can reach 1-5% of the body radius for asteroids, which corresponds to a 2.6 to 13 km thick layer on Vesta (Warren, 2011). Most of this megaregolith may have formed due to a few large impacts, which occurred late in the history of Vesta. Therefore, coverage of megaregolith on early Vesta may have been much thinner and accumulated over time. In this work, we adopt megaregolith depths of 0 km and 5 km as lower and upper

bounds for Vesta.

Assumption of other compositions for the Vestan mantle, such as that of lunar basalts, can result in differences up to a factor of 3 in the radiogenic output power (Haack et al., 1990). Furthermore, the thermal diffusivity of the intact mantle is uncertain to a factor of 1.5-2 (Hanley et al., 1978; Laneuville et al., 2013), while the inclusion of a surface regolith layer with lower conductivity can lower the bulk thermal diffusivity of the brecciated surface layers by ∼40% (Warren, 2011). However, varying these parameters within the stated ranges lead to differences in the resulting temperature profiles smaller than the variations caused by varying the megaregolith thickness between 0 and 5 km. Therefore, our models using these two end-member megaregolith thicknesses provide the full range of likely thermal profiles at a given time. We note that major impact events can excavate deep hot material and have a significant influence on the cooling rate of planetesimals (Davison et al., 2012). This potential effect is not included in our models. Finally, the ascent of magma, which led to the formation of the eucritic surface, may have resulted in more rapid heat transfer through the crust. However, as noted above, our conductive thermal model begins at cessation of convection in Vesta. The extraction of eucritic melts likely occurred quickly after the convective lock up of the Vestan magma ocean when interior crystal fraction was 60-70% (Mandler and Elkins-Tanton, 2013). Therefore, heat transport through the Vestan crust due to melt ascent likely ceased before the complete freezing of the interior and shortly after the cessation of convection.

Once the temperature profile for a given age is found, we then calculate the corresponding initial effective viscosity profile using a stress-dependent Arrhenius-type relationship. Although laboratory experiments on terrestrial mantle rocks can directly constrain viscosities at higher temperatures near the melting point [e.g., $>1200\,^{\circ}$C; Hirth and Kohlstedt (1996)], such results cannot be easily extrapolated down to temperatures relevant to the near-surface of asteroids. In particular, extrapolated viscosities for the oceanic lithosphere at 300-600 $^{\circ}$C appear to be be signficantly higher than required to match the inferred elastic thickness of the oceanic lithosphere beneath seamounts (McNutt and Menard, 1982; Watts and Zhong, 2000). However, due to possible effects of fluids in the oceanic lithosphere, inferred viscosities from seamount-induced deformation may not be fully applicable to dry asteroids such as Vesta. Therefore, we adopt dry olivine viscosities as an upper bound estimate on the viscosity of the Vestan interior (Hirth and Kohlstedt, 1996).

$$\eta(T) = \frac{1}{2} A^{-1} \sigma_{visc}^{-2.5} e^{Q/RT} \text{ Pa s} \quad (7)$$

where A is a constant equal to 4.85×10^4 s^{-1} MPa$^{-3.5}$, Q is the activation energy for dislocation creep, empirically found to be 535 kJ mol^{-1}, T is the temperature, and R is the ideal gas constant. We ignore the pressure dependence of Q since lithostatic pressures characteristic of the Vestan lithosphere are on the order of several 10s MPa. Such pressures increase the value of Q at the 0.1% level (Hirth and Kohlstedt, 1996), which is well below experimental uncertainty and the systemic uncertainties of extrapolation to low temperatures. The viscosity also depends on the applied shear stress σ_{visc}. Because the high viscosity regions of Vesta that govern the rate of viscous relaxation are located in the lithosphere in zones of brittle failure, σ_{visc} is similar to the characteristic shear stresses at the point of brittle failure in the lithophere. We therefore adopt a value of 50 MPa as a typical value for σ_{visc} (see Section 3.1).

Viscosities calculated from equation (7) increase very rapidly at low temperatures, growing by nearly 30 orders of magnitude between 600 °C and 200 °C. Such large viscosity contrasts cannot be reliably solved on our finite element mesh (see Section 2.1). However, materials with sufficiently high viscosity behave as elastic or elasto-plastic solids on a finite timescale, and the calculated deformation field is insensitive to the viscosity chosen for such material (Zhong and Zuber, 2000). The characteristic timescale of deformation is given by $\tau \approx 2\epsilon\eta_{char}/\sigma_{char}$, where ϵ is the strain achieved in timescale τ, η_{char} is a characteristic viscosity, and σ_{char} is a characteristic shear stress. Even for a body significantly out of hydrostatic equilibrium such as present-day Vesta, relaxation to a hydrostatic state corresponds to a strain of ≈0.03 (as discussed below in Section 3.1, the equatorial disequilibrium topography is ∼7 km, which is 0.03 of the radius). Meanwhile, our adopted yield criterion implies maximum lithospheric stresses on the order of 5×10^7 Pa. Adopting 4.5 Gy as the longest relevant timescale, materials with viscosity $\gg 2 \times 10^{26}$ Pa s can be considered free of viscous deformation for the hydrostatic relaxation of Vesta. We therefore truncate all values of viscosity greater than 10^{28} Pa s and set the viscosity at all nodes with higher viscosities to 10^{28} Pa s. These purely temperature-dependent base viscosity profiles are then subject to plasticity correction as described in Section 2.1.

3. Results

3.1. Viscous relaxation

Our conductive cooling models result in temperatures somewhat lower than those at the corresponding times from Ghosh and McSween (1998). By choosing to begin our conductive cooling model after convective shut down, we allow for the possibility that heat generated by short-lived radiogenic isotopes within the first few My after the formation of Vesta was quickly lost via convection. Therefore, the large temperature increases during the first ∼100 My in the conductive models of Ghosh and McSween (1998) do not appear in our model because such high degrees of heating would have triggered efficient convection and rapid cooling within a short early timespan of <1 to several My (see Section 2.2). The global cooling history of Vesta depends strongly on the assumed thickness of the megaregolith layer (Fig. 3). Due to its low thermal conductivity, the megaregolith layer leads to the formation of a boundary layer that can sustain several hundred degrees of temperature contrast and substantially slow the cooling process of the asteroid. The rate of viscous relaxation and the extent of hydrostatic equilibrium are therefore closely tied to assumptions about the thickness of the megaregolith. Specifically, the timespan over which viscous relaxation is a relevant process on Vesta increases significantly with greater megaregolith depth.

In the case of no megaregolith, we simulate the viscous relaxation of Vesta for a range of ages between 15 and 60 My since its initial formation and for a range of non-hydrostaticity. Temperature profiles earlier than these ages are more strongly influenced by the assumption of initial conductive lid thickness. Furthermore, Vesta may have achieved very high degrees of equilibrium (e.g., equatorial bulge amplitude <1 km; see below); however, due to the large number of impacts that have resulted in topography of this amplitude (Marchi et al., 2012), such high degrees of relaxation cannot be maintained throughout solar system history and are not observable today. We therefore exclude very early ages from our relaxation models.

We parameterize departure from hydrostaticity using the disequilibrium factor $f - f_{eq}$. The hydrostatic flattening factor f_{eq} is a function of internal mass distibution and the rotation rate. The rotation rate of early Vesta may have changed several times due to giant impacts with similar magnitudes as the Rheasilvia event (Davison et al., 2013). The true rotation rate for very early Vesta is therefore uncertain. However, the rate of viscous relaxation is a strong function of the difference $f - f_{eq}$ and only weakly dependent on the value of f_{eq} itself (see Section 3.2). We therefore avoid any *a priori*

assumptions about the early rotation rate of Vesta and adopt the present-day rotation period of 5.34 hr to calculate f_{eq} (Russell et al., 2012).

To find the value of f_{eq}, we apply our finite element flow model to a range of trial surface and core flattening factors. For each assumed geometry, we calculate the viscous flow field given uniform viscosity and identify the surface and core flattening factor pair that minimizes internal shear stresses. Note that these uniform viscosity setups are only used to identify the equilibrium flattening; models for viscoplastic relaxation of Vesta use realistic viscosity contrasts as described in Section 2.2. Our method of calculating the equilibrium give identical results compared to first-order analytic theory for small flattening ($f \lesssim 0.1$), in which regime the analytic theory is most valid (Ermakov et al., submitted). Given the modern rotational period and total[2] and core volumes of 7.46×10^{15} and 5.58×10^{15} m^3 (Russell et al., 2012), respectively, the equilibrium flattening factor of the outer surface is $f_{eq} = 0.128 \pm 0.002$ while the core is less oblate at $f_{eq,core} = 0.093 \pm 0.005$. The observed figure of Vesta therefore has a disequibrium factor of 0.065.

We perform our calculations using a range of trial disequilibrium factors potentially relevant to early Vesta. For Relaxation Scenario One (i.e., initial relaxation from non-hydrostatic accreted shape; see Introduction and Fig. 1), the initial accreted shape of Vesta is unknown and the disequilibrium factor may have been very large, potentially greater than the present-day value. For Relaxation Scenario Two (i.e., after an early giant impact), the post-impact non-hydrostaticity was likely similar to that of modern Vesta, which is non-hydrostatic primarily due to two late giant impacts. We therefore adopt a disequilibrium factor of 0.082, which is moderately higher than the modern value, as an upper bound to our range of trial non-hydrostaticities. At the same time, we adopt 0.021 as the lowest trial disequilibrium factor. As discussed above, a large number of impacts capable of excavating >1 km exist on the surface of Vesta (Marchi et al., 2012); therefore, a very closely hydrostatic ancient figure with $f - f_{eq} < 0.021$ would not be readily preserved today.

In all simulations, we assume a core flattening of 0.093. Although this value is correct for the equilbrium figure at the present rotation rate, varying the outer figure of Vesta in principle changes the equilibrium core shape [e.g., Dermott (1979)]. For example, the equilibrium core flattening for the most non-hydrostatic assumed shape ($f - f_{eq} = 0.082$) is 0.12. However, differences in the assumed core figure within this

[2]Total volume is of the best-fit ellipsoid.

range result in negligible variations in the surface relaxation rate.

For $f - f_{eq}$ between 0.021 and 0.082, we find that brittle failure occurred pervasively during Vesta's early evolution. For the no megaregolith case, in the first 15-60 My after convective shut down, the lithosphere of Vesta (defined as the chilled near-surface layer that does not deform viscously over geological timescales) is between 15 and 30 km thick (Fig. 4A). Sufficient stresses build up in the thin lithosphere to imply extensive failure according to Byerlee's rule (Fig. 4B). At these ages for these large values of $f - f_{eq}$, the lithosphere is fully elastoplastic and no purely elastic layer survives (Fig. 4C). In contrast, the deep interior undergoes purely viscous deformation. After accounting for plasticity, effective viscosities in the lithosphere vary across two to three orders of magnitude (Fig. 4C), which is very narrow compared to the >10 orders of magnitude contrast in base viscosity as dictated by the temperature profile alone. Equatorial and polar regions experience higher shear stresses than intermediate latitudes, resulting in more extensive brittle failure and low effective viscosity at greater depths in these regions. Due to the steep temperature and viscosity gradient during Vesta's early history, high shear stresses and brittle failure do not occur beneath an abrupt transition depth, which represents the bottom of the lithosphere. Material beneath this depth behaves as an inviscid fluid in the deformation process while the overlying lithosphere controls the rate of relaxation. The thickness of the plastic layer is primarily a function of the degree of disequilibrium as more strongly non-hydrostatic figures cause more extensive fracturing that penetrates to greater depth.

The rate of viscous relaxation, which is calculated from the flow field after implementation of plasticity (Fig. 4D), for a given degree of disequilibrium decreases rapidly with increasing age (Fig. 5). We can explain the trends in Fig. 5 as follows. At timescales of several 10s to 100 My, the cooling at a given interior position is approximately linear. As such, the characteristic effective viscosity of the plastic layer increases exponentially with age while the rate of relaxation slows correspondingly. The rate of viscous relaxation is also a nearly exponential function of $f - f_{eq}$. As discussed above, the thickness of the plastic layer increases with greater non-hydrostaticity. Given that the temperature profile in the Vestan mantle is nearly linear with respect to depth, the base of the thicker plastic layer samples a region of higher temperature and lower viscosity. Therefore, the characteristic viscosity of the plastic layer decreases rapidly with greater $f - f_{eq}$, resulting in a faster rate of relaxation.

Varying input parameters in the finite element model such as the maximum pre-plasticity viscosity, the maximum allowed viscosity contrast, the mesh refinement, and

the convergence coefficient a results in variations of the final relaxation rate by less than a factor of 2 and typically within 20%. We find these model-dependent uncertainties to be negligible given the much larger variations of relaxation rate with age and $f - f_{eq}$ and systemic uncertainties such as the viscosity model and the adopted thermal diffusivities.

We limit our finite element models to the cases where the equatorial instantaneous relaxation rate is between $\sim$1 and $\sim 10^5$ m My^{-1}. For relaxation rates slower than $\sim$1 m My^{-1}, the relaxation timescale, defined as the amplitude of the non-hydrostatic anomaly (order 10^3 m) divided by the relaxation rate, is longer than 10^3 My, which is far longer than the cooling timescale of Vesta. In such a case, little relaxation is achieved before Vesta has cooled sufficiently to prevent further relaxation. Any configuration with such low relaxation rates would therefore maintain its shape for the age of the solar system, which correspond to a flat trajectory in Fig. 6. Explicit modeling of further shape evolution (i.e., at even lower velocities) becomes unnecessary. On the other hand, the relaxation timescale is $<10^4$ years for instantaneous relaxation rates of $>10^5$ m My^{-1}, implying that relaxation occurs quickly with respect to the cooling timescale of Vesta. In such cases, which correspond to nearly vertical trajectories in Fig. 6, Vesta's figure would relax until a new figure is achieved that has relaxation timescale similar to the cooling timescale. Explicit modeling of cases with higher relaxation velocities (i.e., at higher non-hydrostaticities) is unnecessary as the ultimate figure achieved would remain the same.

Vesta at an earlier age was able to achieve a closely hydrostatic figure (Fig. 6). For the no megaregolith case, Vesta was initially able to relax from a non-hydrostatic accreted shape to a disequilibrium factor $f - f_{eq} \leq 0.02$. This degree of hydrostaticity was maintained for at least the first $\sim$15 My after formation. Although such values of $f - f_{eq}$ are still large compared to that observed on the terrestrial planets, they are similar to the upper bound for unrelaxed global topography on Ceres (Thomas et al., 2005), which is widely considered to be hydrostatically relaxed and is therefore classified as a dwarf planet. If early giant impacts occurred, Vesta would have been able to relax to a more hydrostatic figure than that of the present before $\sim$4.52 Ga, or $\sim$40 My after formation.

A thick megaregolith layer significantly extends the time window in which Vesta was capable of maintaining hydrostatic equilibrium. In the 5-km-thick megaregolith case, $f - f_{eq}$ remained below 0.02 during the first $\sim$80 My while the modern degree of non-hydrostaticity was possible only after $\sim$4.36 Ga (Fig. 6B). The temperature gradient below the megaregolith layer is shallower in the 5 km megaregolith case. Even

so, as in the no megaregolith case, this gradient is sufficiently steep to cause a narrow transition zone (thickness ∼15 km) from a high-viscosity plastic surface layer to an effectively invisicid interior. The 0 km and 5 km megaregolith cases are therefore closely analogous in their rheological structure; the primary difference is that similar temperature profiles correspond to much later ages in the 5 km megaregolith case.

In summary, our finite element flow and conductive cooling models indicate that, with probable extents of internal heating, Vesta should have initially achieved a hydrostatic figure with $f - f_{eq}$ less than 0.02. It then maintained a figure with$f - f_{eq}$ less than the present value of 0.065 during the first 40-200 My after formation, depending on the assumed thickness of megaregolith. Global non-hydrostatic topography of the amplitude observed in the present must have been acquired after this early hydrostatic epoch, implying that the Veneneia and Rheasilvia impact basins post-date 40-200 My after formation.

3.2. Relic hydrostatic terrains

Our viscous relaxation models suggest that Vesta achieved a nearly hydrostatic global figure early during its history and raise the possibility that hydrostatic terrains from early Vesta are present on the surface of the asteroid today. Although Vesta was subject to two late giant impact events, terrains far from these impact basins may have remained largely undisturbed until the present and may reflect the morphology of Vesta's early hydrostatic surface. The northern hemisphere of Vesta shows high crater densities. Some regions (the heavily cratered terrains or HCTs) are at or near crater saturation and may date to the first several 100s My after Vesta's formation (Marchi et al., 2012). Furthermore, unsaturated regions adjacent to the HCTs exhibit few craters larger than ∼50 km, suggesting that they may still faithfully preserve ancient topography at the longest wavelengths.

At the same time, giant impact simulations suggest that ejecta from the Rheasilvia basin-forming event created a belt of increased crustal thickness near the present-day equator and that surface topography north of this equatorial ridge likely underwent minimal modification [e.g., Jutzi and Asphaug (2011); Jutzi et al. (2013); Ivanov and Melosh (2012)]. Crustal thickness maps derived from Bouguer gravity anomalies show a clear ring of high crustal thickness in the equatorial region [Fig. 7A; Ermakov et al. (submitted)]. The terrain to the north of this belt exhibits significantly more subdued topography than the surface inside the impact basins, which is consistent with a relative absence of major reshaping due to large impacts in this region (Fig. 7B).

We identify the region north of the equatorial belt of high crustal thickness as a likely relic hydrostatic surface from Vesta's early history. We isolate this region and fit its topography to a tri-axial ellipsoid with center position, orientation, and length of the the three principle axes as fit parameters (Bertoni, 2010). We find that the best-fit tri-axial ellipsoid approximates an oblate ellipsoid of revolution with similar equatorial radii and a significantly shorter polar radius (Table 1). The volume of this best-fit rotational ellipsoid is 1.9% larger than that of the present shape, which is fully consistent with the expected volume of ancient Vesta before the more recent giant impacts (Schenk et al., 2012). Furthermore, we find a large negative offset between the observed and fitted figures in the z direction (i.e., parallel to the rotation axis), which is consistent with the remove of material from the southern hemisphere by the giant impacts. The fitted parameters of the tri-axial ellipsoid are robust with respect to small variations in the regions chosen for the fit.

As expected, the residual topography in the northern undisturbed terrains is subdued (Fig. 7B). Most of the undisturbed terrains are within 5 km of the fitted surface. This residual topography is regional in scale, with wavelengths on the order of 100 - 300 km. Such topography, if it dates to the early period of rapid global scale hydrostatic relaxation, would not have relaxed fully due to its relatively small spatial scale compared to the degree-2 non-equilibrium modeled in this work. For these reasons, the fitted northern ellipsoid likely represents a faithful description of the pre-giant impacts global figure of Vesta.

The best-fit rotational ellipsoid corresponds to a flattening of $f_{ancient}$ =0.147±0.001, which is greater than that of the equilibrium figure for the present-day rotation period. Using a similar numerical grid search method as used above to find the hydrostatic flattening of Vesta, we find that this flattening factor implies a paleo-rotation period of 5.02±0.01 hr, which implies 6.3% despinning due to late impacts. The flattening of the core is expected to be f_{core} =0.104±0.001, with equatorial and polar radii of 114.0 and 102.2 km, respectively. The polar axis of the fitted ellipsoid is offset by 3.0° from the modern rotational axis. The stated errors are due to the discrete nature of the numerical, equilibrium figure-finding algorithm and do not include contribution from uncertainty in the interior density distribution.

This set of rotational parameters was established no later than 40-200 My after Vesta's formation, depending on the depth of megaregolith, and may represent Vesta's primordial spin state if very early giant impacts did not occur. The small amount of despinning suggests that large asteroids such as Vesta had initial rotation rates similar

to those observed in the present day, which has been suggested by previous theoretical work (Schlichting and Sari, 2007).

To assess the effect of varying the rotation rate on our relaxation simulations, we repeated a finite element relaxation simulation using the newly derived period of 5.02 hr (instead of 5.34 hr) to obtain f_{eq}. A model run at 40 My after convective shut down shows that, for the same disequilibrium $f - f_{eq}$, using the new f_{eq} increased the instantaneous relaxation velocity by a factor of 2.3 (Fig. 5A). This difference is similar to that resulting from changing model parameters (see Section 3.1) and is small compared to the two to four orders of magnitude differences resulting from changing the disequilibrium $f - f_{eq}$. Increasing all relaxation velocities by a factor of 2.3 does not significantly alter the resulting relaxation paths or the length of the time window of efficient relaxation. Furthermore, the possibility of large early impacts (see Section 1) implies that the rotation period of early Vesta may have been higher or lower than 5.02 hr. As described above, we therefore avoid *a priori* assumptions and use 5.34 hr to calculate f_{eq}.

4. Discussion

The high efficiency of viscous relaxation on early Vesta implies that global scale non-hydrostatic features such as the relatively unrelaxed Venenia and Rheasilvia giant impact basins formed after the initial epoch of intense heating. Depending on the assumed thickness of megaregolith, global topography of the amplitude observed today is possible only after 4.52-4.36 Ga. The two giant impacts on Vesta therefore must have occurred after this age, which is consistent with observed crater densities in the basin floors (Schenk et al., 2012). These model crater retention ages indicate that the older of the two basins, Veneneia, formed at ∼2.1 Ga. By this time, core temperatures in Vesta would have fallen below 450°C even for the 5 km megaregolith layer case. The viscosity of silicates at the core-mantle boundary therefore would have been in excess of 10^{30} Pa s, which does not allow viscous relaxation on solar system timescales. Therefore, the pre-giant impact flattening of the core (f_{core} =0.104±0.001) would be maintained into the present day, assuming that the giant impacts did not directly alter the core shape.

The longest principal axis of the best-fit ellipsoid trends towards the western edge of Vestalia Terra, which is likely an ancient mascon that predates the giant impacts and may date to the early magmatic epoch of Vesta's history within the first ∼100 My of its formation (Raymond et al., 2013; Buczkowski et al., 2013). This asymmetry in the pre-impact figure of Vesta provides additional support for a primordial origin for Vestalia

Terra. Due to the regional scale of Vestalia Terra, which spans ∼60° in latitude and ∼100° in longitude (Jaumann et al., 2012), and the possibility of anomalously rigid local rheology as evidenced by the absence of crosscutting grooves (Buczkowski et al., 2013), Vestalia Terra was not subject to the global-scale viscoplastic relaxation modeled in this work (Anderson and O'Connell, 1967). Future regional relaxation models of Vestalia Terra can potentially constrain the rheological structure of early Vesta and place an upper bound on the degree of heating beneath this region.

The 5.02 hr period derived from the fit to the northern undisturbed terrains implies that late impacts have resulted in ∼6.3% despinning. Assuming that the core was in hydrostatic equilibrium with the pre-impact rotation rate and outer figure (both approximated by ellipsoids of revolution) and that the core and silicate proportions of Vesta have densities of 7450 and 3100 kg m^{-3}, respectively, the pre-impact angular momentum of the Vesta was 2.58×10^{27} kg m^2 s^{-1}. The post-impact angular momentum of Vesta, assuming that the core maintains its fossil, pre-impact shape and orientation and that the surface is the best-fit ellipsoid of revolution (Russell et al., 2012), is 2.45×10^{27} kg m^2 s^{-1}. The bulk of this difference in angular momentum must have been delivered by the late Veneneia and Rheasilvia impactors. We estimate the upper limit of the angular momentum delivered in one such impact. Assuming a diameter of 66 km, velocity of 5400 m s^{-1} (Jutzi et al., 2013), and density of 3000 kg m^{-3} for the Rheasilvia impactor, its maximum angular momentum is 0.17×10^{27} kg m^2 s^{-1} for an impact at 75°S latitude (Schenk et al., 2012). This contribution alone is sufficient to account for the change in Vesta angular momentum. Combined with a contribution of similar magnitude from the Veneneia impactor, the amount of despinning inferred from our fit to the undisturbed northern terrains is consistent with possible angular momentum transfer due to late giant impacts. Given the moderate probability of early giant impacts that can deliver a similar amount of angular momentum as the Veneneia and Rheasilvia basin-forming impactors, the rotation rate of Vesta since its formation at 2-6 My after CAIs (Tang and Dauphas, 2012) has likely remained close (i.e., of order 6%) to that of the present.

In addition to despinning, both giant impacts may have led to significant true polar wander. Under the assumption of a single impact basin with axisymmetric geometry, Matsuyama and Nimmo (2011) showed that reorientation of <20° and despinning of <20% are consistent with Hubble Space Telescope topography data available at the time. These values are fully consistent with our estimate based on undisturbed terrain morphology. However, the model does not provide accurate estimates of the

non-axisymmetric coefficients of Vesta's gravity field, C_{22} and S_{22} (F. Nimmo, personal communication), indicating that the impacts led to a more asymmetrical mass redistribution than assumed or that other effects, such as the pre-existing Vestalia Terra mascon, had introduced significant azimuthal asymmetry. Given new constraints on Vesta's gravity coefficients and the morphology of its giant impacts basins and overall shape, the range of plausible reorientation and despinning may require revision.

Our results indicate that other large asteroids that underwent extensive early heating may have also experienced significant global relaxation. Ground-based observations of Ceres provide evidence for central mass concentration although not necessarily full igneous differentiation with a metallic core (Thomas et al., 2005). The hydrostatically relaxed figure of Ceres may be due to intense early heating and viscous relaxation as described here for Vesta. Alternatively, the near-surface composition of Ceres may be sufficiently rich in low viscosity materials such as water ice or hydrated silicates to allow viscous relaxation without strong heating (Castillo-Rogez and McCord, 2010; Dombard and Schenk, 2013; Bland, 2013). We note that the rheological profile of Ceres may be fundamentally different from that of Vesta in that the lowest viscosity material may be present at the surface due to compositional variation whereas the most inviscid material in Vesta is at depth due to the temperature gradient. Therefore, short wavelength features on Ceres may be able to relax readily while only the longest wavelength topography on Vesta, which is senstive to the rheology of the deep interior, is likely to approach hydrostatic equilibrium.

The third most massive asteroid, Pallas, is a near-twin of Vesta in terms of overall size ($\sim$532 km mean diameter). Like Vesta, the surface of Pallas is characterized by large, apparently unrelaxed impact basins (Schmidt et al., 2009). However, unlike for Vesta, no strong evidence exists for early igneous differentiation in Pallas. Its density has been estimated to be between 2400 and 3300 kg m^{-3} (Schmidt et al., 2009; Standish and Hellings, 1989), which is consistent with both differentiated material and undifferentiated chondritic material. The unrelaxed impact basins on Pallas may therefore be late acquisitions after an early hydrostatic epoch or primordial features in the case of weak interior heating. More detailed mapping of Pallas in the future and the potential identification of terrains on Pallas consistent with ancient hydrostatic surfaces would imply the early heating and differentiation of the body and the late age of large impact basins. As with the northern hemisphere of Vesta, such relic hydrostatic terrains are expected to show saturation crater densities, lack of major impact resurfacing, and freedom from topographic features due to distal giant impact basins such as a belt of

thickened crust. Furthermore, an unconstrained ellipsoid fitted to purported hydrostatic terrains must produce plausible values for flattening and total volume.

The morphology of the southern hemisphere of asteroid Iris has been mapped in detail using radar observations (Ostro et al., 2010). In contrast to Vesta, Ceres, and Pallas, the surface of Iris appears to be highly irregular at all scales >30 km with topographic relief of ∼20% of the body radius (the corresponding value for the Rheasilvia basin is ∼6%). No region that can be closely fitted to a rotational ellipsoid similar to the undisturbed terrains on Vesta is definitively observed on Iris, although a large portion of the body still has not been mapped at high resolution. Furthermore, Iris' low density (2660 kg m^{-3}) and surface spectra consistent with that of ordinary chondrites do not suggest extensive early heating. Iris may have therefore never experienced sufficient interior heating to reach hydrostatic equilibrium similar to Vesta and Ceres. Its high non-hydrostaticity may then be due to a combination of late impacts and a primordial irregular surface acquired during accretion.

Among smaller bodies, the asteroid Lutetia (mean diameter ∼100 km) is suspected to have undergone significant internal heating due to its high observed density (3400 kg m^{-3}), which requires anomalously low macroporosity or reduction of interior microporosity through sintering or melting (Pätzold et al., 2011; Weiss et al., 2011). However, sintering alone implies minimum temperatures of 760-950°C in the deep interior while the lithosphere may remain cold and resistant to deformation (Wieczorek et al., 2013; Fu and Elkins-Tanton, submitted). As discussed above, such temperatures imply characteristic internal viscosities too high to allow viscous relaxation. The highly irregular shape of Lutetia is therefore consistent with early interior sintering.

5. Conclusions

We use finite element calculations coupled with conductive cooling models to constrain the extent of early global relaxation expected for the asteroid Vesta. Given likely degrees of internal heating as dictated by both thermal evolution models and remote sensing data, Vesta was able to undergo relaxation towards hydrostatic equilibrium. Vesta reached a highly hydrostatic figure shortly after accretion with a maximum non-hydrostatic equatorial bulge amplitude of <2 km during the first 15 to 80 My after formation. Vesta then maintained a figure closer to hydrostatic equilibrium than its present one during at least the first 40 My after formation. Inclusion of a thick megaregolith layer can extend this hydrostatic epoch to 200 My after formation. The Veneneia

and Rheasilvia impact basins, which are essentially unrelaxed, must have occurred after this early hydrostatic epoch.

The efficient hydrostatic relaxation of early Vesta motivates the possibility of finding relic hydrostatic terrains on its present-day surface. We isolate a large region in the northern hemisphere based on its ancient crater retention ages, lack of large impact features, and location away from structures associated with the southern hemisphere giant impacts. The best-fit ellipsoid for this region indicates a pre-impact rotation period of 5.02 hr, which implies a cumulative 6.3% reduction in angular velocity due to the two late giant impacts. This rotation rate was established at some time less than 40-200 My after Vesta's formation and would represent the primordial rotation rate of Vesta if very early giant impacts did not occur. Other asteroids that experienced intense early heating and rapid cooling may also have undergone early hydrostatic relaxation. As such, the potential observation of similar hydrostatic terrains on other asteroids would provide constraints on the degree of early interior heating.

Acknowledgments

We thank C. A. Raymond, F. J. Ciesla, B. P. Weiss, F. Nimmo, W. B. McKinnon, B. E. Mandler, and B. W. Denevi for a range of discussions that helped to improve the manuscript. We also thank W. Bangerth and G. Kanschat for their kind assistance with the deal.II finite element library. R. R. F. thanks the NSF Graduate Research Fellowship program for support.

References

Aggarwal, H., Oberbeck, V., 1979. Monte carlo simulation of lunar megaregolith and implications. In: Lunar and Planetary Science Conference Proceedings. Vol. 10. pp. 2689–2705.

Albert, R., Phillips, R., Dombard, A., Brown, C., 2000. A test of the validity of yield strength envelopes with an elastoviscoplastic finite element model. Geophys. J. Int. 140 (2), 399–409.

Amelin, Y., Krot, A. N., Hutcheon, I. D., Ulyanov, A. A., 2002. Lead isotopic ages of chondrules and calcium-aluminum-rich inclusions. Science 297 (5587), 1678–1683.

Anderson, D. L., O'Connell, R., 1967. Viscosity of the earth. Geophysical Journal of the Royal Astronomical Society 14 (1-4), 287–295.

Bangerth, W., Hartmann, R., Kanschat, G., 2007. deal. ii- a general-purpose object-oriented finite element library. ACM T. Math. Software 33 (4), 24.

Bangerth, W., Kronbichler, M., 2008. The step-22 tutorial program. `http://www.dealii.org/developer/doxygen/deal.II/step-22.html`.

Berckhemer, H., Kampfmann, W., Aulbach, E., Schmeling, H., 1982. Shear modulus and Q of forsterite and dunite near partial melting from forced-oscillation experiments. Phys. Earth. Planet. Int. 29 (1), 30–41.

Bertoni, B., 2010. Multi-dimensional ellipsoidal fitting. Tech. Rep. SMU-HEP-10-14, Department of Physics, Southern Methodist University.

Binzel, R. P., Xu, S., 1993. Chips off of asteroid 4 vesta: Evidence for the parent body of basaltic achondrite meteorites. Science 260 (5105), 186–191.

Bland, M. T., 2013. Predicted crater morphologies on Ceres: Probing internal structure and evolution. Icarus 226, 510–521.

Brace, W. F., Kohlstedt, D. L., 1980. Limits on lithospheric stress imposed by laboratory experiments. J. Geophys. Res. 85 (11), 6248–6252.

Buczkowski, D. L., De Sanctis, M. C., Raymond, C. A., Wyrick, D. Y., Ammannito, E., Frigeri, A., Williams, D., Russell, C., 2013. Brumalia tholus: An indication of magmatic intrusion on Vesta? In: Lunar and Planetary Science Conference Abstracts. Vol. 1719. p. 1996.

Byerlee, J., 1978. Friction of rocks. Pure App. Geophys. 116 (4), 615–626.

Castillo-Rogez, J. C., McCord, T. B., 2010. Ceres' evolution and present state constrained by shape data. Icarus 205 (2), 443–459.

Chambat, F., Ricard, Y., Valette, B., 2010. Flattening of the Earth: further from hydrostaticity than previously estimated. Geophys. J. Int. 183 (2), 727–732.

Chambers, J. E., 2004. Planetary accretion in the inner solar system. Earth Planet. Sci. Lett. 223 (3), 241–252.

Davison, T., Ciesla, F., Collins, G., 2012. Post-impact thermal evolution of porous planetesimals. Geochim. Cosmochim. Acta.

Davison, T. M., O'Brien, D. P., Ciesla, F. J., Collins, G. S., 2013. The impact histories of meteorite parent bodies. Meteor. Planet. Sci., 1–25.

De Sanctis, M., Ammannito, E., Capria, M., Tosi, F., Capaccioni, F., Zambon, F., Carraro, F., Fonte, S., Frigeri, A., Jaumann, R., et al., 2012. Spectroscopic characterization of mineralogy and its diversity across Vesta. Science 336 (6082), 697–700.

Denevi, B. W., Coman, E. I., Blewett, D. T., Mittlefehldt, D. W., Buczkowski, D. L., Combe, J. P., de Sanctis, M. C., Jaumann, R., Li, J. Y., Marchi, S., et al., 2012. Regolith depth, mobility, and variability on Vesta from Dawn's low altitude mapping orbit. In: Lunar and Planetary Science Conference Abstracts. Vol. 43. p. 1943.

Dermott, S. F., 1979. Shapes and gravitational moments of satellites and asteroids. Icarus 37 (3), 575–586.

Dombard, A. J., McKinnon, W. B., 2006. Elastoviscoplastic relaxation of impact crater topography with application to ganymede and callisto. J. Geophys. Res.: Planets 111 (E1).

Dombard, A. J., Schenk, P. M., 2013. The giant cue ball: Efficient relaxation of Ceres' craters. In: Lunar and Planetary Science Conference Abstracts. Vol. 1719. p. 1798.

Elkins-Tanton, L. T., Weiss, B. P., Zuber, M. T., 2011. Chondrites as samples of differentiated planetesimals. Earth Planet. Sci. Lett. 305, 1–10.

Ermakov, A., Zuber, M. T., Smith, D. E., Raymond, C. A., Balmino, G., Fu, R. R., Ivanov, B. A., submitted. The gravity field of Vesta. Icarus.

Fu, R. R., Elkins-Tanton, L. T., submitted. The fate of magmas in planetesimals and the retention of primitive chondritic crusts. Earth Planet. Sci. Lett.

Ghosh, A., McSween, H. Y., 1998. A thermal model for the differentiation of asteroid 4 vesta, based on radiogenic heating. Icarus 134 (2), 187–206.

Haack, H., Rasmussen, K. L., Warren, P. H., 1990. Effects of regolith/megaregolith insulation on the cooling histories of differentiated asteroids. J. Geophys. Res. 95 (B4), 5111–5124.

Hanley, E., Dewitt, D., Roy, R., 1978. The thermal diffusivity of eight well-characterized rocks for the temperature range 300–1000 K. Eng. Geol. 12, 31–47.

Hevey, P. J., Sanders, I. S., 2006. A model for planetesimal meltdown by 26Al and its implications for meteorite parent bodies. Meteorit. Planet. Sci. 41, 95–106.

Hirth, G., Kohlstedt, D. L., 1996. Water in the oceanic upper mantle: implications for rheology, melt extraction and the evolution of the lithosphere. Earth Planet. Sci. Lett. 144 (1), 93–108.

Hoffmann, M., Nathues, A., Vincent, J., Sierks, H., 2012. Unique crater morphologies on Vesta, and the context of a deep regolith and intermediate gravity. In: EGU General Assembly Conference Abstracts. Vol. 14. p. 5530.

Housen, K. R., Wilkening, L. L., Chapman, C. R., Greenberg, R., 1979. Asteroidal regoliths. Icarus 39 (3), 317–351.

Ivanov, B., Melosh, H., 2012. The rheasilvia crater on vesta: Numerical modeling. In: Lunar and Planetary Science Conference Abstracts. Vol. 43. p. 2148.

Jaumann, R., Williams, D. A., Buczkowski, D. L., Yingst, R. A., Preusker, F., Hiesinger, H., Schmedemann, N., Kneissl, T., Vincent, J. B., Blewett, D., et al., 2012. Vesta's shape and morphology. Science 336 (6082), 687–690.

Johnson, T. V., McGetchin, T. R., 1973. Topography on satellite surfaces and the shape of asteroids. Icarus 18 (4), 612–620.

Jutzi, M., Asphaug, E., 2011. Mega-ejecta on asteroid Vesta. Geophys. Res. Lett. 38 (1), L01102.

Jutzi, M., Asphaug, E., Gillet, P., Barrat, J.-A., Benz, W., 2013. The structure of the asteroid 4 Vesta as revealed by models of planet-scale collisions. Nature 494 (7436), 207–210.

Kaus, B. J., 2010. Factors that control the angle of shear bands in geodynamic numerical models of brittle deformation. Tectonophysics 484 (1), 36–47.

King, S., Hager, B., 1990. The relationship between plate velocity and trench viscosity in newtonian and power-law subduction calculations. Geophys. Res. Lett. 17 (13), 2409–2412.

Konopliv, A., Asmar, S., Park, R., Bills, B., Centinello, F., Chamberlin, A., Ermakov, A., Gaskell, R., Rambaux, N., Raymond, C., Russell, C., Smith, D., Tricarico, P.,

MT, Z., submitted. The vesta gravity field, spin pole and rotation period, landmark positions, and ephemeris from the dawn tracking and optical data.

Laneuville, M., Wieczorek, M., Breuer, D., Tosi, N., 2013. Asymmetric thermal evolution of the moon. J. Geophys. Res.: Planets.

Mandler, B. E., Elkins-Tanton, L. T., 2013. The origin of eucrites, diogenites, and olivine diogenites: Magma ocean crystallization and shallow magma chamber processes on vesta. Meteoritics & Planetary Science.

Marchi, S., McSween, H., O'Brien, D., Schenk, P., De Sanctis, M., Gaskell, R., Jaumann, R., Mottola, S., Preusker, F., Raymond, C., et al., 2012. The violent collisional history of asteroid 4 Vesta. Science 336 (6082), 690–694.

Matsuyama, I., Nimmo, F., 2011. Reorientation of Vesta: Gravity and tectonic predictions. Geophys. Res. Lett. 38 (14), L14205.

McCord, T. B., Adams, J. B., Johnson, T. V., 1970. Asteroid Vesta: Spectral reflectivity and compositional implications. Science 168 (3938), 1445–1447.

McCoy, T. J., Mittlefehldt, D. W., Wilson, L., 2006. Asteroid differentiation. Meteorites and the early solar system II 1, 733–745.

McNutt, M. K., Menard, H., 1982. Constraints on yield strength in the oceanic lithosphere derived from observations of flexure. Geophys. J. Roy. Astr. S. 71 (2), 363–394.

Melosh, J. H., 1977. Global tectonics of a despun planet. Icarus 31 (2), 221–243.

Morbidelli, A., Bottke, W., Nesvorný, D., Levison, H. F., 2009. Asteroids were born big. Icarus 204 (2), 558–573.

Moresi, L. N., Solomatov, V., 1995. Numerical investigation of 2D convection with extremely large viscosity variations. Phys. Fluids 7, 2154.

Neumann, W., Breuer, S., Spohn, T., submitted. Differentiation of vesta: Implications for a shallow magma ocean. Earth Planet. Sci. Lett.

Ostro, S., Magri, C., Benner, L., Giorgini, J., Nolan, M., Hine, A., Busch, M., Margot, J., 2010. Radar imaging of asteroid 7 Iris. Icarus 207 (1), 285–294.

Pätzold, M., Andert, T. P., Asmar, S. W., Anderson, J. D., Barriot, J. P., Bird, M., Häusler, B., Hahn, M., Tellmann, S., Sierks, H., et al., 2011. Asteroid 21 Lutetia: low mass, high density. Science 334 (6055), 491–492.

Pohánka, V., 2011. Gravitational field of the homogeneous rotational ellipsoidal body: a simple derivation and applications. Contrib. Geophys. Geodes. 41 (2), 117–157.

Poitrasson, F., Halliday, A., Lee, D.-C., Levasseur, S., Teutsch, N., 2004. Iron isotope differences between Earth, Moon, Mars and Vesta as possible records of contrasted accretion mechanisms. Earth Planet. Sci. Lett. 223 (3), 253–266.

Raymond, C. A., Park, R. S., Asmar, S. W., Konopliv, A. S., Buczkowski, D. L., De Sanctis, M. C., McSween, H. Y., Russell, C. T., Jaumann, R., Preusker, F., 2013. Vestalia Terra: An ancient mascon in the southern hemisphere of Vesta. Vol. 1719. p. 2882.

Reddy, V., Nathues, A., Le Corre, L., Sierks, H., Li, J. Y., Gaskell, R., McCoy, T., Beck, A. W., Schröder, S. E., Pieters, C. M., et al., 2012. Color and albedo heterogeneity of Vesta from dawn. Science 336 (6082), 700–704.

Righter, K., Drake, M. J., 1997. A magma ocean on Vesta: Core formation and petrogenesis of eucrites and diogenites. Meteor. Planet. Sci. 32 (6), 929–944.

Russell, C., Raymond, C., Coradini, A., McSween, H., Zuber, M., Nathues, A., De Sanctis, M., Jaumann, R., Konopliv, A., Preusker, F., et al., 2012. Dawn at Vesta: Testing the protoplanetary paradigm. Science 336 (6082), 684–686.

Sanderson, C., 2010. Armadillo: An open source C++ linear algebra library for fast prototyping and computationally intensive experiments. Tech. rep., NICTA.

Schenk, P., O'Brien, D. P., Marchi, S., Gaskell, R., Preusker, F., Roatsch, T., Jaumann, R., Buczkowski, D., McCord, T., McSween, H. Y., et al., 2012. The geologically recent giant impact basins at Vesta's south pole. Science 336 (6082), 694–697.

Schlichting, H., Sari, R., 2007. The effect of semicollisional accretion on planetary spins. Astrophys. J. 658 (1), 593.

Schmidt, B., Thomas, P., Bauer, J., Li, J. Y., McFadden, L., Mutchler, M., Radcliffe, S., Rivkin, A., Russell, C., Parker, J. W., et al., 2009. The shape and surface variation of 2 Pallas from the Hubble Space Telescope. Science 326 (5950), 275–278.

Schultz, R. A., 1993. Brittle strength of basaltic rock masses with applications to Venus. J. Geophys. Res. 98 (E6), 10883–10.

Solomatov, V., 2000. Fluid dynamics of a terrestrial magma ocean. Origin of the Earth and Moon 1, 323–338.

Šrámek, O., Milelli, L., Ricard, Y., Labrosse, S., 2011. Thermal evolution and differentiation of planetesimals and planetary embryos. Icarus 217 (1), 339.

Standish, E. M., Hellings, R. W., 1989. A determination of the masses of Ceres, Pallas, and Vesta from their perturbations upon the orbit of Mars. Icarus 80 (2), 326–333.

Sterenborg, M. G., Crowley, J. W., 2012. Thermal evolution of early solar system planetesimals and the possibility of sustained dynamos. In: Lunar and Planetary Science Conference Abstracts. Vol. 43. p. 2361.

Tang, H., Dauphas, N., 2012. Abundance, distribution, and origin of< sup> 60</sup> fe in the solar protoplanetary disk. Earth Planet. Sci. Lett. 359–360, 248–263.

Thomas, P., Parker, J. W., McFadden, L., Russell, C. T., Stern, S., Sykes, M., Young, E., 2005. Differentiation of the asteroid Ceres as revealed by its shape. Nature 437 (7056), 224–226.

Turcotte, D. L., Schubert, G., 2002. Geodynamics. Cambridge Univ Pr.

Warren, P. H., 2011. Ejecta–megaregolith accumulation on planetesimals and large asteroids. Meteor. Planet. Sci. 46 (1), 53–78.

Warren, P. H., Rasmussen, K. L., 1987. Megaregolith insulation, internal temperatures, and bulk uranium content of the Moon. J. Geophys. Res. 92 (B5), 3453–3465.

Watts, A., Zhong, S., 2000. Observations of flexure and the rheology of oceanic lithosphere. Geophys. J. Int. 142 (3), 855–875.

Weidenschilling, S. J., 2011. Initial sizes of planetesimals and accretion of the asteroids. Icarus 214 (2), 671–684.

Weiss, B. P., Elkins-Tanton, L. T., Antonietta Barucci, M., Sierks, H., Snodgrass, C., Vincent, J. B., Marchi, S., Weissman, P. R., Pätzold, M., Richter, I., Fulchignoni, M., Binzel, R. P., Schulz, R., 2011. Possible evidence for partial differentiation of asteroid Lutetia from Rosetta. Planet. Space Sci. 152, 341–390.

Wieczorek, M. A., Neumann, G. A., Nimmo, F., Kiefer, W. S., Taylor, G. J., Melosh, H. J., Phillips, R. J., Solomon, S. C., Andrews-Hanna, J. C., Asmar, S. W., et al., 2013. The crust of the moon as seen by grail. Science 339 (6120), 671–675.

Yamaguchi, A., Taylor, G. J., Keil, K., 1996. Global crustal metamorphism of the eucrite parent body. Icarus 124 (1), 97–112.

Zhong, S., Zuber, M. T., 2000. dependent compensation of surface topography. J. Geophys. Res. 105 (E2), 4153–4164.

Zuber, M. T., Smith, D. E., Lehman, D. H., Hoffman, T. L., Asmar, S. W., Watkins, M. M., 2013a. Gravity Recovery and Interior Laboratory (GRAIL): Mapping the lunar interior from crust to core. Space Sci. Rev., 1–22.

Zuber, M. T., Smith, D. E., Watkins, M. M., Asmar, S. W., Konopliv, A. S., Lemoine, F. G., Melosh, H. J., Neumann, G. A., Phillips, R. J., Solomon, S. C., et al., 2013b. Gravity field of the Moon from the Gravity Recovery and Interior Laboratory (GRAIL) mission. Science 339 (6120), 668–671.

6. Figures

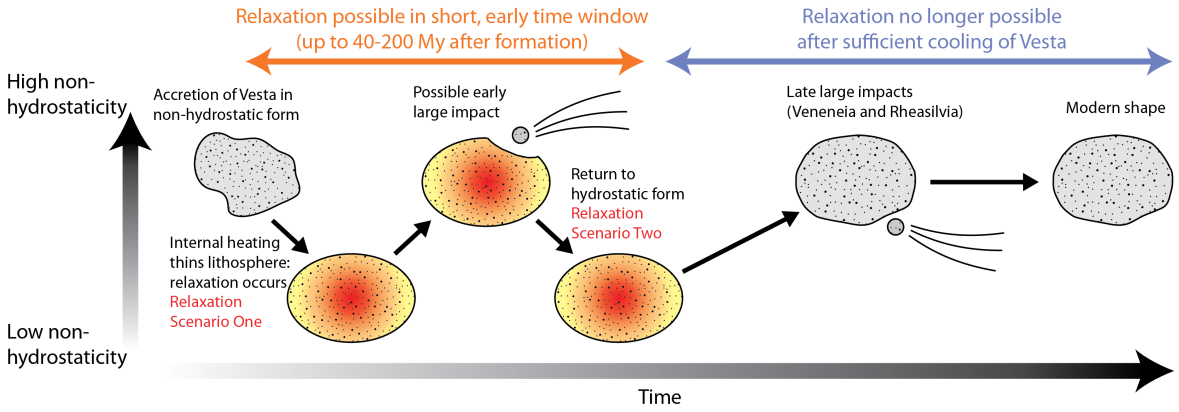

Figure 1: Schematic illustration of the evolution of Vesta's long wavelength topography. Upon formation, rapid internal heating (denoted by red-yellow coloration) due to short-lived radiogenic isotopes lead to a differentiated interior with a thin, cold lithosphere. Vesta therefore reached a highly hydrostatic figure with a non-hydrostatic equatorial bulge amplitude of <2 km (see Section 3.1). If early large impacts disturbed the figure of Vesta, subsequent relaxation would restore a high hydrostaticity. By 40-200 My after formation, the Vestan interior had cooled sufficiently to prevent relaxation to a figure more hydrostatic than that of the present day. The late Veneneia and Rheasilvia basin-forming impacts occurred after this transition, thereby imparting a significant non-hydrostatic component to Vesta's observed figure.

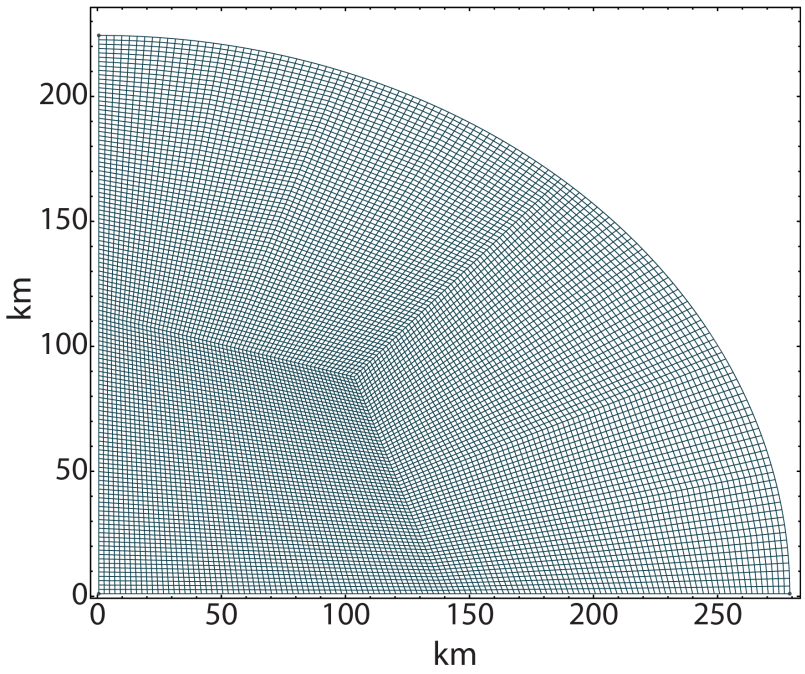

Figure 2: Example of a finite element mesh used in our viscoplastic flow simulations. The x- and y-axes represent the equatorial and polar axes, respectively, while the outer figure is one quarter of an ellipse. The mesh shown consists of 12288 cells and corresponds to a flattening of f=0.19, which is the observed present day value for Vesta.

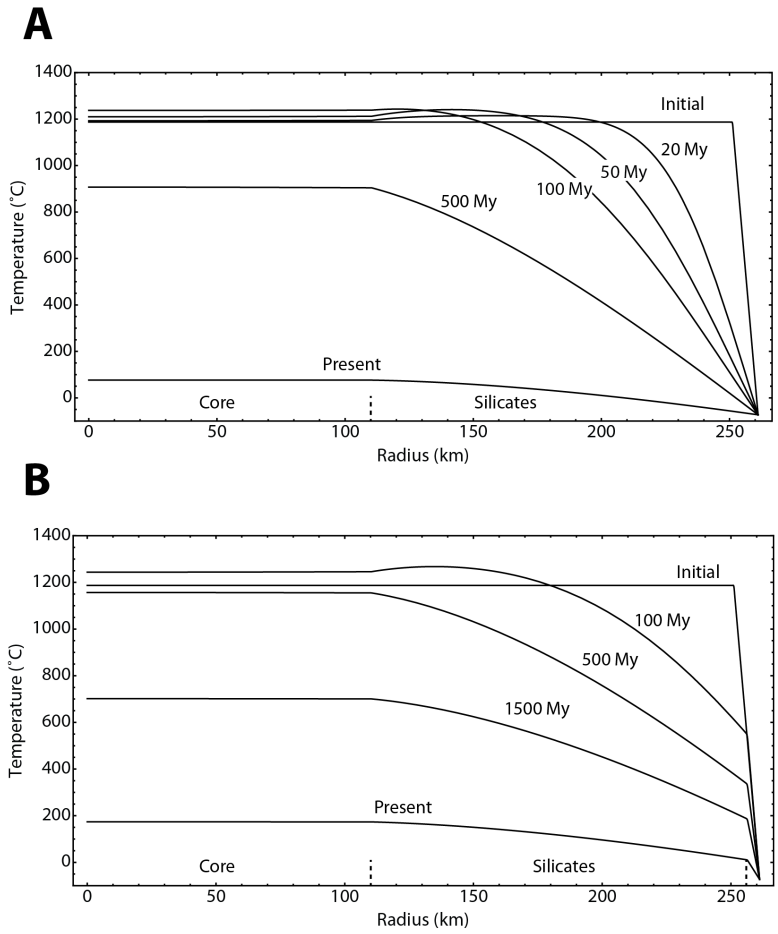

Figure 3: Thermal evolution of Vesta assuming (**A**) no megaregolith and (**B**) 5 km thick megaregolith. The assumed initial temperature profile consists of an isothermal interior at 1200°C underlying a 10 km conductive lid with a linear temperature profile. Decay of long-lived radioisotopes cause initial heating in the deep interior. Dashed line segments on the x-axis indicate the interfaces between the core, intact silicates, and megaregolith layers.

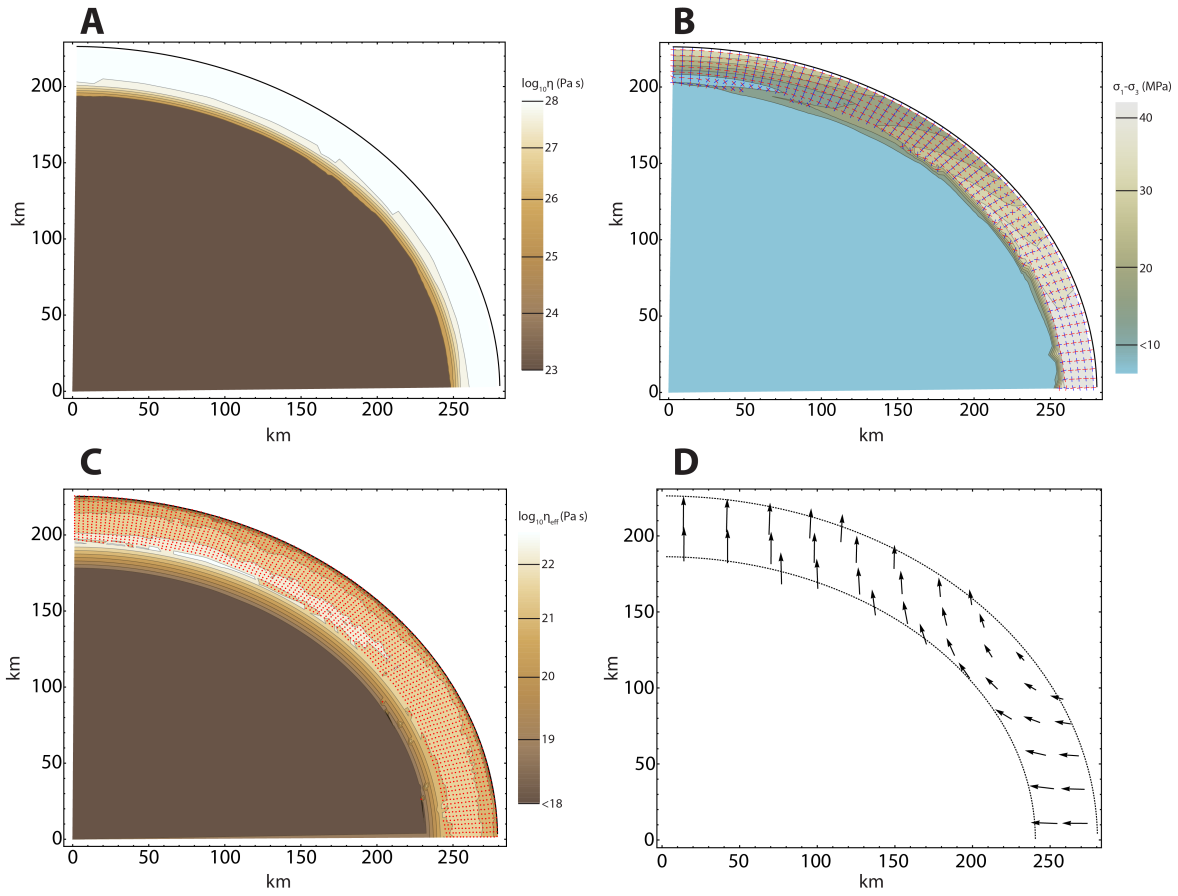

Figure 4: Initial setup and converged result of an individual viscous relaxation model run. The geometry and thermal structure shown correspond to Vesta with its present day shape (f=0.19) at 30 My after convection shut down. The vertical and horizontal axes represent the polar axis and equator, respectively. (**A**) The initial viscosity structure based directly on the thermal profile. Viscosities above 10^{28} Pa s and below 10^{23} Pa s are set to those values, respectively (see Section 2.2). (**B**) Shear stress ($\sigma_1 - \sigma_3$) field corresponding to the initial viscosity. Blue and red segments mark the direction of the more and less compressive stress in the r-z plane, respectively. One set of segments is plotted for every fourth finite element for clarity. Note that the direction of σ_1 and σ_3 may be in the azimuthal direction. Stress in large portions of the lithosphere imply failure according to Byerlee's rule. The effective viscosities at these failing locations are therefore iteratively reduced to simulate plastic deformation until shear stresses do not lead to additional failure anywhere (see Section 2.1). (**C**) Converged effective viscosity field after iterative adjustment of local viscosity at points of brittle failure to reflect plasticity shows a limited effective viscosity range in the lithosphere and a thin transition zone to an effectively inviscid deep interior. Red points indicate cells where brittle failure occurred. Stresses at all finite element nodes imply no additional failure (according to Byerlee's rule). (**D**) The resulting viscous flow field in the lithosphere reflects the excess initial flattening. Vector length is directly proportional to local flow velocity. The longest vector represents a velocity of 20.0 km My^{-1}.

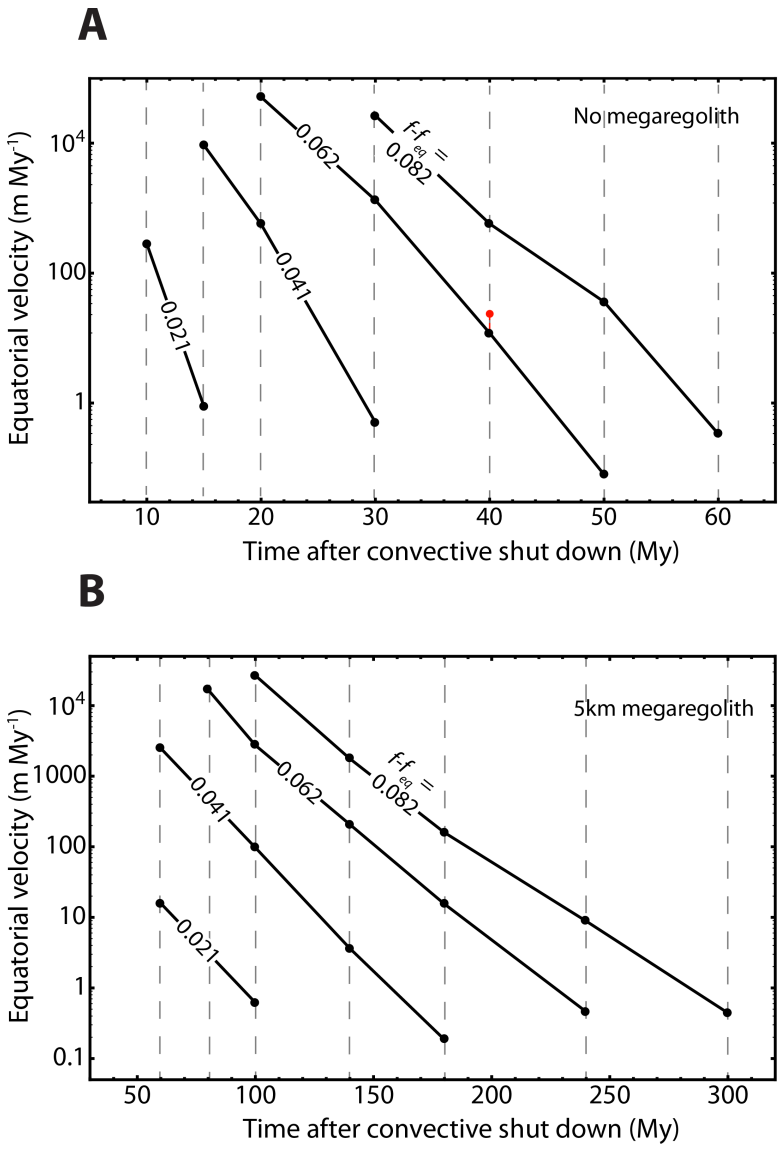

Figure 5: Relaxation rate of viscous flow at the equator as a function of age and non-hydrostaticity for (**A**) no megaregolith and (**B**) 5 km megaregolith. Black dots represent results of individual numerical simulations. Flow velocity varies nearly exponentially with both age and degree of disequilibrium. Note that evolution in relaxation velocity occurs over a much longer timescale in the case of a thick megaregolith. Red point in part (A) indicates velocity calculated using a 5.02 hr period to obtain f_{eq} instead of 5.34 hr.

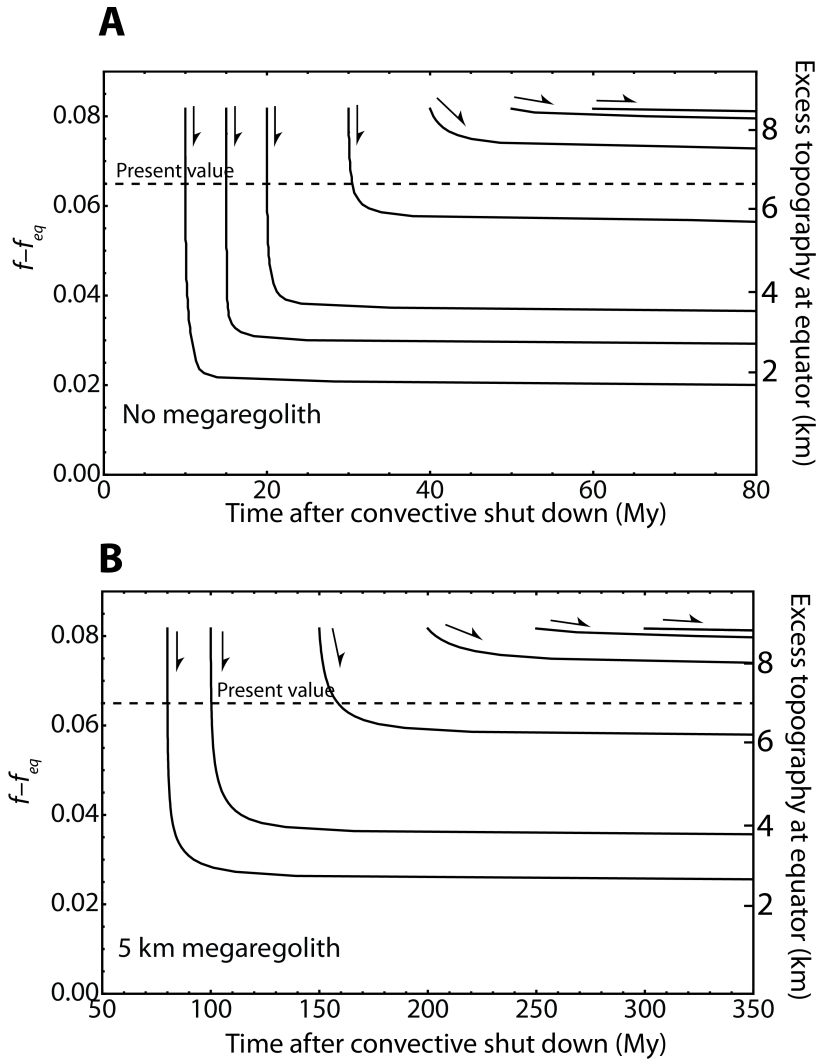

Figure 6: Possible relaxation paths of Vesta at a range of ages for (**A**) no megaregolith and (**B**) 5 km megaregolith. Vesta was able to relax to more hydrostatic figures during its earliest history. The observed present-day disequilibrium ($f - f_{eq}$ =0.062) was only possible after ≈4.52 Ga for the no megaregolith case and ≈4.36 Ga for 5 km megaregolith. Note that there is no constraint on whether Vesta followed any particular path. These projected relaxation paths indicate the amplitude of non-hydrostatic topography that could be supported by the Vestan lithosphere at each time: the disequilibrium factor at which each path bottoms out is the amount of non-hydrostaticity that could be sustained at the initial age for that path.

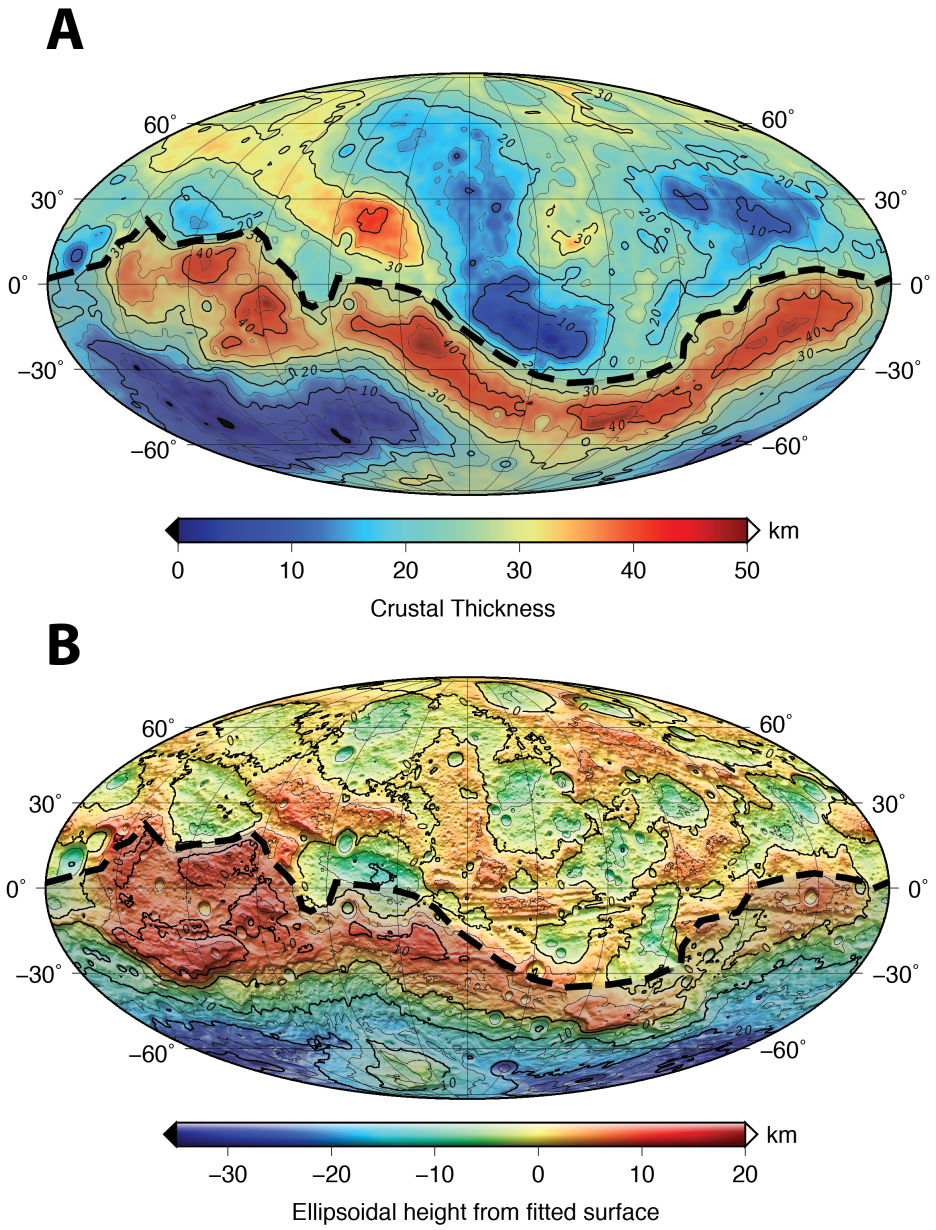

Figure 7: Definition of fitted region and residuals for the ellipsoid fit to the northern undisturbed terrains. (**A**) Crustal thickness map from Ermakov et al. (submitted) showing the undisturbed terrains (north of dashed boundary) used to fit to a triaxial ellipsoid. The belt of high crustal thickness near the equator is a consequence of one or both giant impact events near the present-day south pole. Terrains north of this belt show near-saturation cratering density and likely have not suffered significant disruption since the early history of Vesta when viscious relaxation was rapid. Note that crustal thicknesses shown here are relative and that absolute crustal thickness cannot be uniquely determined for Vesta (Ermakov et al., submitted). (**B**) Residual topography of the ellipsoid fit as defined by the difference between the observed surface of Vesta and the fitted ellipsoid along a line normal to the fitted surface. Bold and light black contours indicate 10 and 5 km intervals, respectively. Residuals within the northern undisturbed terrains are below 10 km, in contrast to the terrains to the south. Southern terrains are lightly shaded in both panels for clarity.

7. Tables

Radii (km)			Center offset (km)			Axes orientations		
a (km)	b (km)	c (km)	Δx	Δy	Δz	a	b	c
280.6	274.6	236.8	-0.8	-0.2	-5.7	λ=17.3°	λ=107.3°	λ=-177.3°
						ϕ=2.9°	ϕ=-0.8°	ϕ=87.0°

Table 1: The results of fitting the northern undisturbed terrains to a tri-axial ellipsoid with unconstrained position and orientation. The angles λ and ϕ refer to the planetocentric east longitude and latitude, respectively, of the intersection of the principal axis of the fitted ellipsoid and the surface of Vesta. Both the center offset values and the angles λ and ϕ are given in the Claudia coordinate system (Russell et al., 2012).